The heterogeneity of mudflat erodibility

Article *in* Geomorphology · August 2019

DOI: 10.1016/j.geomorph.2019.106834

7 authors, including:

Qin Zhu
GuangDong University of Technology
13 PUBLICATIONS **125** CITATIONS
SEE PROFILE

B. Van Prooijen
Delft University of Technology
47 PUBLICATIONS **520** CITATIONS
SEE PROFILE

Debora Cynthia Maan
Delft University of Technology
5 PUBLICATIONS **15** CITATIONS
SEE PROFILE

Zheng Bing Wang
Delft University of Technology
204 PUBLICATIONS **3,294** CITATIONS
SEE PROFILE

Geomorphology 345 (2019) 106834

Contents lists available at ScienceDirect

Geomorphology

journal homepage: www.elsevier.com/locate/geomorph

The heterogeneity of mudflat erodibility

Q. Zhu [a,b,c], B.C. van Prooijen [b], D.C. Maan [b], Z.B. Wang [a,b,d], P. Yao [f], T. Daggers [e], S.L. Yang [a,*]

[a] State Key Laboratory of Estuarine and Coastal Research, East China Normal University, Shanghai, China
[b] Department of Hydraulic Engineering, Delft University of Technology, Delft, the Netherlands
[c] Institute of Environmental and Ecological Engineering, Guangdong University of Technology, Guangdong, China
[d] Deltares, Delft, the Netherlands
[e] Department Estuarine & Delta Systems, Royal Netherlands Institute for Sea Research, Yerseke, the Netherlands
[f] College of Harbor, Coastal and Offshore Engineering, Hohai University, Nanjing, China

ARTICLE INFO

Article history:
Received 9 November 2018
Received in revised form 27 July 2019
Accepted 31 July 2019
Available online 02 August 2019

Keywords:
Erosion threshold
In situ measurement
Mudflat
Diatoms
Erosion rate
Storm

ABSTRACT

The prediction of the erosion of mudflats is hampered by inaccurate estimates of the erodibility distribution of the sediment bed. To investigate how erodibility varies in space and what the vertical distribution over the sediment depth is, comprehensive observations of the sediment properties, hydrodynamics and bed-level changes were conducted on an intertidal flat in the Western Scheldt Estuary, the Netherlands. The erosion potential on a mudflat is determined by the critical shear stress for erosion (τ_e), erosion rate coefficient (M) and local hydrodynamic conditions. A clear difference in hydrodynamic forcing was observed, leading to significant bed level variations at the low water line, where erosion often occurs during very shallow water condition, and a nearly constant bed level at the upper part. The erosion parameters τ_e and M could be determined over a sediment bed of 12 cm at the low water line. The erosion coefficient M can be considered constant with depth, although there is a large spreading. A clear vertical variation of τ_e was found: τ_e increased significantly downward from 0.10 Pa at the sediment surface to 1.13 Pa at 12 cm below the surface. Additionally, there was a strong indication that the presence of diatoms enhanced τ_e in the upper 2 mm of sediment by five times of the abiotic τ_e (from 0.09 Pa to 0.46 Pa). These findings lead to the following improvement for predicting morphological changes of tidal mudflats: (1) very shallow conditions should be better simulated, (2) the vertical distribution of τ_e should be considered. Otherwise, erosion rates can be overestimated, especially during extreme events, because exposure of the deeper well-consolidated layer likely occurs; and (3) an appropriate description of the effect of diatoms should be considered as part of the bottom boundary condition.

1. Introduction

Tidal flats play a key role in estuarine ecosystems and are important buffers against coastal flooding (Costanza et al., 1997; Goodwin et al., 2001; Barbier et al., 2008). However, tidal flats are threatened by anthropogenic interventions (e.g., upstream damming, storm surge barriers and deepening of navigation channels) and by climate change (e.g., accelerated sea level rise); see Chu et al. (2006); Yang et al. (2006); Blum and Roberts (2009); Andersen et al. (2011); Wang et al. (2015); Yang et al. (2015); de Vet et al. (2017). Predicting the response of tidal flats to these interventions and climate changes forms an important aspect of the assessments of management scenarios. Predictions of the morphological evolution of tidal flats are however not straightforward, as it is a complex outcome of tidal currents, waves, bed and suspended sediment properties, and even ecological processes. They rely on a number of assumptions, like considering a one-dimensional cross-section only, or simplifying the effects of waves and the heterogeneity of bed sediment properties, see e.g. van der Wegen et al. (2017), Maan et al. (2018).

Various steps have been taken to overcome all shortcomings of these models. In this paper, we focus on a specific aspect, namely the erosion rate formulation and its parameters. The erosion rate in these models is often calculated based on the so-called Partheniades' erosion equation, which is expressed as:

$$E = M(\tau_{cw} - \tau_e) \quad \text{or} \quad E = M'\left(\frac{\tau_{cw}}{\tau_e} - 1\right) \text{for} \tau_{cw} > \tau_e \tag{1}$$

where E (kg/(m^2 s)) is the erosion rate, M (s/m) and M' (kg/(m^2 s)) are the erosion coefficients, τ_{cw} is the total bed shear stress under the combined wave–current action, and τ_e is the critical shear stress for erosion. In many model studies, the empirical erosion parameters M (or M') and τ_e are specified as constants. However, these two parameters vary with the sediment characteristics (e.g., sediment composition, bulk density, consolidation state) and even with biological interactions (Mitchener

* Corresponding author.
E-mail address: slyang@sklec.ecnu.edu.cn (S.L. Yang).

https://doi.org/10.1016/j.geomorph.2019.106834
0169-555X/

and Torfs, 1996; Le Hir et al., 2007; van Prooijen et al., 2011). Recently, efforts have been taken to study the relationship between erosion threshold of sand-mud mixture with porosity and grain size distribution, mainly the mud fraction (van Rijn, 2007; Wu et al., 2018; Yao et al., 2018). The values of τ_e and M have been proven to be site-dependent and to vary over wide ranges (Whitehouse, 2000; Winterwerp et al., 2012). The tuning of their values determines the applicability of existing models in simulating the sediment transport in estuarine and coastal areas, and above all, the realism of the erosion law (Ge et al., 2015).

The estimation of the erosion threshold has remained a challenge (Andersen et al., 2007; van Prooijen and Winterwerp, 2010; Salehi and Strom, 2012). Efforts have been made over the last two decades to measure the erodibility of sediment beds; see the summary by Le Hir et al. (2008). Measurements in laboratory flumes have been performed using artificial kaolinite or homogenous mixtures to study the effect of cohesion on the bed strength (Mehta and Partheniades, 1982; Gomez and Amos, 2005; Jacobs et al., 2011). However, the sediment beds in these experiments were not similar to real sediment beds. Other studies have used an alternative approach: an undisturbed sediment core is placed in an erosion device, and a controlled forcing is imposed on the sediment surface (e.g., Gust and Morris, 1989; Schünemann and Kühl, 1993; Austen et al., 1999; Bohling, 2009; Dickhudt et al., 2009; van Maren et al., 2009). In addition, in situ annular flumes have been used directly on sediment beds (Amos et al., 1992; McNeil et al., 1996; Widdows et al., 1998; Houwing, 1999; Tolhurst et al., 1999; Paterson et al., 2000; Neumeier et al., 2006; Ravens, 2007). These devices aimed to determine the resuspension characteristics, but were always difficult to operate and time-consuming (Le Hir et al., 2008). In contrast to the various flumes/devices with unidirectional flows, Andersen et al. (2007) determined the critical erosion shear stress by comparing time series of the bed shear stress and bed-level changes in high frequency (also see Verney et al., 2007; Salehi and Strom, 2012; Shi et al., 2015). This approach, as also applied in this study, yields the erosion thresholds of the surface sediment layers exposed to water and requires accurate estimations of the bed shear stress under natural wave–current action.

The erosion thresholds for coarser particles, such as sand and gravel, can be estimated for known grain size distributions (Shields, 1936). However, when the sediment bed is dominated by mud (grain size ≤ 63.5 μm), the sediments are stabilized by cohesive forces caused by the surface charges acting on each particle (Kuti and Yen, 1976; Amos et al., 1996; Taki, 2001). van Ledden (2003) proposed a clay (grain size ≤ 3.9 μm) content of 7% (with a constant silt/clay ratio for a certain system) as the transition between cohesive and non-cohesive mixtures. A lower critical shear stress for erosion has often been related to a lower bulk density of relatively freshly deposited mud (Mehta, 1988; Delo and Ockenden, 1992; Armanini, 1995; Mitchener and Torfs, 1996; Taki, 2001).

The biological effects on the erosion threshold of mud beds are also important (Andersen et al., 2005; Le Hir et al., 2007). Generally, microphytobenthos act as stabilizers because they form a biofilm by producing extracellular polymeric substances (EPS) that protect the sediment surface against hydrodynamic forces (Austen et al., 1999; Riethmüller et al., 2000; de Brouwer et al., 2005; Andersen et al., 2010). Meso- and macrozoobenthos are mainly destabilizers. For instance, the benthic bivalve *Macoma balthica* is a bioturbator whose burrowing and feeding activities increase the sediment erosion potential (Willows et al., 1998; Widdows et al., 2000; van Prooijen et al., 2011), and the mud snail *Hydrobia ulvae* increases the erodibility by increasing the bed roughness and egesting organic pellets that are easily eroded (Andersen and Pejrup, 2002; Orvain et al., 2003; Orvain et al., 2007).

The literature overview as given above indicates the uncertainties in the definitions of the erosion rates and its parameters. It also shows a lack of direct estimations from field measurements. Furthermore, many lab experiments are based on cores exposed to (uniform channel) flow. The response of the bed to waves is not considered. We therefore set up a field campaign to determine the erosion rates in-situ for realistic flow and wave conditions.

Three frames were placed on a mud flat to relate the bed erosion potential in both the cross-shore and vertical dimensions with hydrodynamic forcings. Instruments were mounted on the frames to measure the wave and current regimes, suspended sediment concentration (SSC), bed sediment properties, and bed-level. In this way, we could: (1) quantify the spatial and temporal variability of critical shear stress of an undisturbed natural mud bed; (2) estimate the influence of biota on erosion threshold; and (3) determine the stability of a semi-enclosed mud bed in a natural wave–current environment. This paper aims to improve the input of erosion parameters in the erosion modules of fine-grained bed morphodynamic models.

The paper is organized as follows. Section 2 gives an overview of the study area, the mudflat in the Western Scheldt, the Netherlands. The measurement campaign is described in Section 3. This section provides the definitions of variables and parameters as well. Results are shown in Section 4. The interpretation and discussion of the results follows in Section 5. This section also provides a discussion of the implications of the results. Conclusions are drawn in Section 6.

2. Study area

In situ measurements were carried out on the Kapellebank mudflat, a semi-enclosed tidal flat along the north bank of the Western Scheldt Estuary in the Netherlands (Fig. 1b). The tidal flat has a long-shore length of 1.8 km and a cross-shore length of 0.9 km. The tidal flat faces a channel to the south. The tide is semi-diurnal with a mean tidal range of approximately 4.5 m, which indicates a macrotidal regime. The bed slope of the flat is mild (ca. 3‰). The dominant wind direction is southwest, leading to wind waves exposure of Kapellebank. The average wave height in the adjacent channel is about 0.15 m (Maan et al., 2018). Our measurements and previous measurements showed that the bed sediment of this area is dominated by mud (Kuijper et al., 2004). From early spring until the onset of summer, 80% of the surface of the intertidal flat is covered by a visible brown biofilm that forms a hummock-hollow pattern (Fig. 1e; Weerman et al., 2011).

The observation sites were located on a transect perpendicular to the channel (Fig. 1c). The lowest site, Site A1, was located at the interface between the intertidal flat and the channel (51°27′24″N, 3°58′21″E) at an elevation of −1.84 m NAP (Amsterdam Ordnance Datum, approximately MSL) (Fig. 1d). The bed elevations of sites A2 (51°27′30″N, 3°58′24″E) and A3 (51°27′37″N, 3°58′27″E) were −0.98 m and −0.25 m NAP, respectively.

3. Material and methods

3.1. Data collection

The observations were carried out from April 28 to May 25, 2014. Wave-logger (OSSI-010-003C, Ocean Sensor Systems, Inc., USA), ADV (Acoustic Doppler Velocity meter, 6.0 MHz Vector current meter, Nortek AS, Norway) and fluorometers (C3™ Submersible Fluorometer, Turner Designs, USA) were deployed at three sites (Table 1). In the laboratory, the suspended sediment collected in the field was fully mixed with water, whose turbidity was measured by fluorometers used in the field. The suspended sediment concentration (SSC) of each mixture was measured. The relationship between SSC values and turbidities from indoor calibration was used to convert in situ turbidity readings to SSC (Fig. A1).

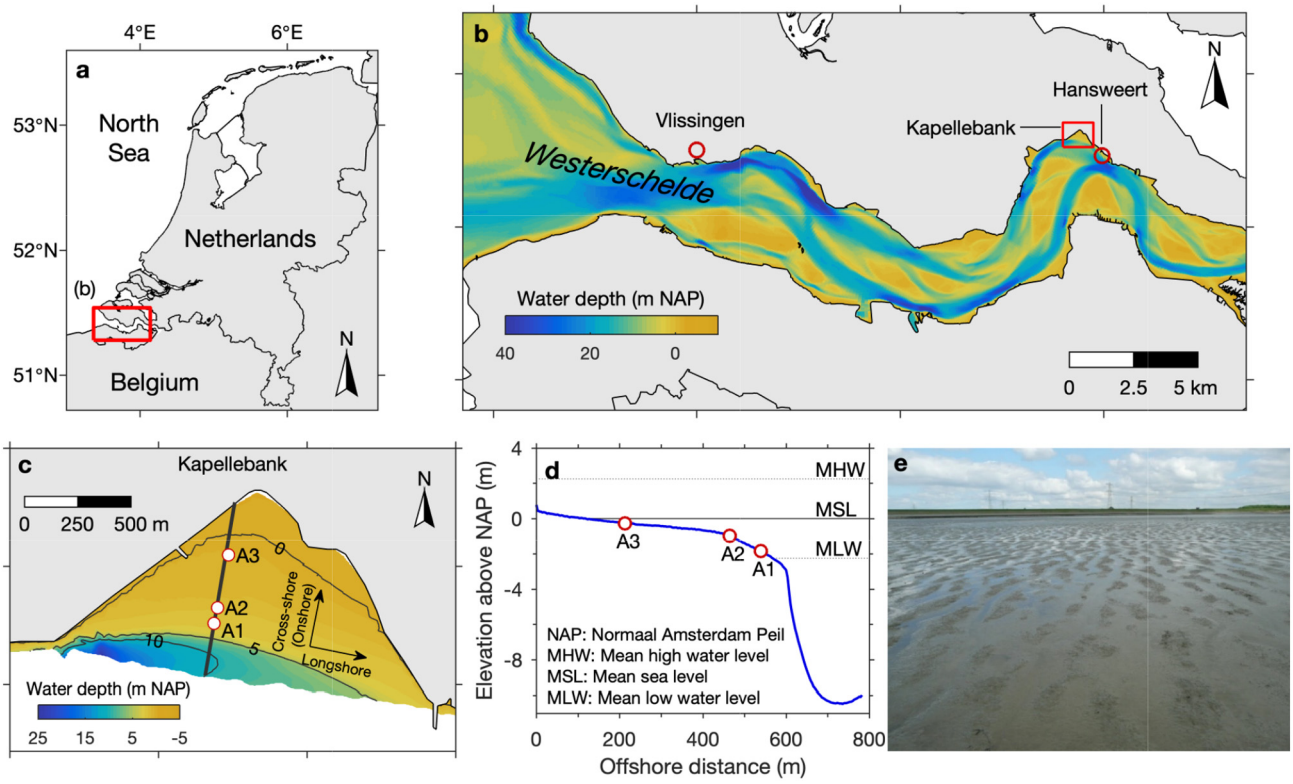

Fig. 1. (a) Map of the Netherlands; (b) map of the Western Scheldt Estuary, which shows the locations of the study area, Vlissingen (meteorological station), and Hansweert (water level gauge); (c) map of the Kapellebank mudflat, which shows the observation sites, bathymetry as measured from jet skis (Shore Monitoring & Research, the Netherlands), cross- and long-shore dimensions; (d) the cross-shore bathymetry profile with the site locations; and (e) photograph shows a visible hummock-hollow pattern from diatoms.

Time series of the predicted and measured water levels every 10 min at the Hansweert gauge (Fig. 1b) were provided by Rijkswaterstaat (part of the Dutch Ministry of Infrastructure and the Environment), the Netherlands. Hourly mean wind speed, wind direction, air pressure, and sunshine duration data at the Vlissingen meteorological station (Fig. 1b) were obtained from the Royal Netherlands Meteorological Institute (KNMI).

The surface sediment at each site was sampled as a mixture of at least five scrapes of the uppermost 2 mm of the bed sediment at the three observation sites on April 29. To minimize the sediment samples being dried or wet, we took samples directly after the tidal flat was exposure to the air, and each sediment sample was taken on dry area or ripple crest if there was rippled micro-morphology. The water content and grain size distribution of the fresh sediment samples were measured. Wet sediment samples were weighed and oven dried at a temperature of 60 °C until a stable weight was reached (≥96 h). The water content W was derived as the ratio of the weight of the water (the difference between the wet and dry sediment weights) to the dry sediment weight. The grain size distributions of the sediment samples were analyzed using a laser diffraction particle size analyzer (Mastersizer 2000, Malvern Instruments Ltd., UK). Before the grain size measurement, organic matter and carbonate were removed from the sediment samples by HCl and H_2O_2. Then the samples were disaggregated by the addition of $(NaPO_3)_6$ and subsequent ultrasonic treatment.

Chlorophyll *a* concentrations were measured as a proxy for the diatom biomass in the bed sediment. Sediment samples were collected from the upper 2 mm of the sediment near site A2 (approximately 70 m from site A2) on April 28. Two and three samples were collected at points that visually appeared to have high and low diatom biomass, respectively, and 6 samples were collected at random points. At each point, a pooled sample consisting of ten cores with a total surface area of 17.7 cm^2 was collected (total surface area per point = 3.5 cm^3). The samples were stored on ice until being transferred to a −80 °C freezer. The chlorophyll *a* concentrations were determined after freeze drying

Table 1
Instrumentation and sampling schemes.

Parameters	Instrument	Sampling scheme	Sites
Waves	Wave-logger	Pressure probe was 5 cm above the bed; 4096 samples at 10 Hz every 20 min.	A1
3D velocity	ADV	Sampling volume (2.2 cm^3) at 15 cm above the bed; April 28–May 2: 2048 samples at 8 Hz every 5 min; May 3–May 24: 720 samples at 8 Hz every 10 min.	A1, A2, A3
Relative bed-levels	ADV	Measuring the distance between the transmitter and the sediment surface every 5 or 10 min with an accuracy of ±1 mm.	A1, A2, A3
Turbidity	Fluorometer	Probe 15 cm above the bed; Measure every 5 min.	A1

and extraction in 90% acetone by high-performance liquid chromatography (HPLC; Wright et al., 1991).

3.2. Calculation of the bed shear stress

The total bed shear stress due to the combined wave–current action, τ_{cw} (Pa), was calculated with the wave–current interaction model (Soulsby, 1997):

$$\tau_{cw,rms} = \sqrt{\tau_m^2 + \frac{1}{2}\tau_w^2}, \text{where} \tau_m = \tau_c\left[1 + 1.2\left(\frac{\tau_w}{\tau_c + \tau_w}\right)^{3.2}\right] \quad (2)$$

$$\tau_{cw,\,max} = \sqrt{(\tau_m + \tau_w|\,\cos\phi_{cw}|)^2 + (\tau_w|\,\sin\phi_{cw}|)^2} \quad (3)$$

in which τ_w (Pa) and τ_c (Pa) are the wave-induced and current-induced bed shear stresses, respectively, and ϕ_{cw} is the angle between current and wave directions. Here we use root-mean-square value ($\tau_{cw,rms}$) when it is used in erosion model, because the consequence of total bed shear stress over the wave-cycle is considered. Maximum bed shear stress ($\tau_{cw,max}$) is used when determining erosion threshold.

The wave-induced bed shear stress, τ_w, was obtained by analyzing the high-frequency pressure data measured by the wave-logger. Variations due to air pressure were first removed. The wave parameters (significant wave height H_s and significant wave period T_s) were obtained using linear wave theory (Tucker and Pitt, 2001). At the edge of the wave boundary layer, the peak orbital excursion ($\hat{A}_\delta$) and peak orbital velocity ($\hat{U}_\delta$) can be expressed as (van Rijn, 1993):

$$\hat{A}_\delta = \frac{H_s}{2\,\sinh(kh)} \quad (4)$$

$$\hat{U}_\delta = \omega\hat{A}_\delta = \frac{\pi H_s}{T_s\,\sinh(kh)} \quad (5)$$

in which $k = 2\pi/L$, $L = (gT^2/2\pi)\tanh(kh)$ (m^{-1}) is the wave length, k is the wave number, h (m) is the water depth, and ω (s^{-1}) is the wave frequency.

The time-averaged (over a wave cycle) bed shear stress due to waves, τ_w (Pa), is expressed as (van Rijn, 1993):

$$\tau_w = \frac{1}{4}\rho_w f_w \hat{U}^2{}_\delta \quad (6)$$

where ρ_w (kg/m^3) is the water density, and f_w (−) is the friction coefficient, which is defined by the diagram of hydraulic regimes of oscillatory flow (van Rijn, 1993, Fig. A2):

$$f_w = \begin{cases} 2\ \mathrm{Re}_w^{-0.5}, \textit{laminar} \\ 0.09\ \mathrm{Re}_w^{-0.2}, \textit{smooth turbulent} \\ \min\left[\exp(-6 + 5.2r^{-0.19}), 0.3\right], \textit{rough turbulent} \end{cases} \quad (7)$$

where $\mathrm{Re}_w = \frac{\hat{U}_\delta\hat{A}_\delta}{\nu}$ (−) and $r = \frac{\hat{A}_\delta}{k_s}$ (−) are the wave Reynolds number and relative roughness, respectively, k_s is the Nikuradse roughness, which is given by $k_s = 2.5d_{50}$, where d_{50} is the median grain size of the bed sediment, and ν (m^2/s) is the kinematic viscosity of water. Eq. (6) applies to skin friction. Note that in our case, the laminar regime was most often found in normal weather, and the smooth turbulent regime was found at shallow water ($h < 2$ m) during storm condition.

The variance in the turbulent velocity fluctuation in the vertical dimension $\overline{w_t^2}$ is used to infer the current-induced bed shear stress, τ_c, using the following formulation:

$$\tau_c = C\rho_w\overline{w_t^2} \quad (8)$$

in which the constant C is assumed to be 0.19 (Stapleton and Huntley, 1995). Because measured near-bed velocities might be affected by surface wave motion in tidal areas, wave–turbulence decomposition is applied (Zhu et al., 2016). Here, the Energy Spectrum Analysis (ESA) approach was used to obtain $\overline{w_t^2}$. The ESA approach was developed by Soulsby and Humphery (1990) to divide the variance without separating the instantaneous time series.

The current direction and the wave direction were obtained from the burst-mean velocities and decomposed wave orbital velocities, respectively; see Zhu et al. (2016).

3.3. Empirical models to determine the erosion threshold and erosion coefficient

Two approaches to determine the erosion threshold, which is represented by the critical bed shear stress for erosion (τ_e), are used in this paper. In the first approach, the erosion threshold is determined by the bed shear stress at the moment that the bed starts or stops degrading (Andersen et al., 2007). Time series of the bed shear stress and bed-level variation are estimated from the field measurements. In this study, the sediment bed was relatively stable during calm weather, and there was a period without bed deposition, with maximum erosion depth of 11.4 cm, during the storm condition. We define the stable bed level before bed degradation as the original bed surface (depth $z = 0$). When a τ_e value is determined, the difference between the original bed surface level and the bed level at this moment is defined as the depth where the τ_e is determined. The vertical distribution of τ_e with depth z is therefore obtained.

In the second approach, the critical bed shear stress for erosion is calculated using the bed properties (van Rijn, 2007). The critical bed shear stress (τ_e) is calculated based on the median grain size of the sediment bed (d_{50}):

$$\tau_e = \begin{cases} \left(\frac{c_{gel}}{c_{gel,s}}\right)\left(\frac{d_{sand}}{d_{50}}\right)^{\gamma}\tau_{cr}, d_{50}<62.5\ \mu\text{m (mud)} \\ \left(1 + p_{clay}\right)^3\tau_{cr}, d_{50}\geq 62.5\ \mu\text{m (sand)} \end{cases} \quad (9)$$

in which, c_{gel} is the dry bulk density, $c_{gel,s}$ is the dry bulk density of sand bed by mass (1722 kg/m^3, assuming that porosity of the sand bed equals to 0.35); γ is the empirical coefficient, in the range of 1–2 (1.5 for this study); p_{clay} is the clay fraction; τ_{cr} is the critical bed shear stress based on a parametric Shields curve, for $D_* \leq 4$, $\theta_{cr} = 0.115D_*{}^{-0.5}$ and $\tau_{cr} = [(\rho_s - \rho_w)gd_{50}]\theta_{cr}$, with D_* of dimensionless particle size of the bed sediment. Flume study shows that Eq. (9) performs well when calculating τ_e for the mud bed with rich silt (silt content is about 60% in our study, Yao et al., 2015).

The bed level change rate is $\frac{\Delta\eta}{\Delta t} = \frac{1}{\rho_{dry}}(D - E + A)$, where $\Delta\eta$ is the bed level variation in the time period Δt, ρ_{dry} (kg/m^3) is the dry density of surficial sediment, A is advection term, and D and E are the deposition rate and erosion rate, respectively:

$$E = \begin{cases} M\cdot(\tau_{cw,rms} - \tau_e), \tau_{cw} > \tau_e \\ 0, \tau_{cw} \leq \tau_e \end{cases} \quad (10)$$

$$D = \begin{cases} 0, \tau_{cw} > \tau_d \\ \omega_s c_b\left(1 - \frac{\tau_{cw}}{\tau_d}\right), \tau_{cw} \leq \tau_d \end{cases} \quad (11)$$

where ω_s and c_b are settling velocity (m/s) of suspended sediment and suspended sediment concentration (kg/m^3). Arguments have been raised about the necessity of including a critical bed-shear stress for deposition, τ_d (Dyer, 1986; Sanford and Halka, 1993; Lumborg, 2005; Winterwerp, 2007). Especially in the review of Sanford and Halka (1993) various arguments are used in favor and against the use of a

critical bed shear stress for deposition. Here we adopt the option of using τ_d for the following reason. Deposition is assumed to stop when τ_{cw} exceeds a certain threshold, which is the critical shear stress for deposition, τ_d. Strong eddy diffusivity, which is proportional to the shear velocity, leads to a greater upward diffusion flux than the downward settling flux (Maa et al., 2008). In Eq. (11), this process can be simplified as deposition being prohibited when the bed shear stress exceeds τ_d. τ_d is often regarded smaller than or equal to τ_e (Christie et al., 1999; Lumborg, 2005). In this case, during the pure erosion stage, when $\tau_{cw} > \tau_e$, $E > 0$ and $D = 0$. The bed level change rate $\Delta\eta/\Delta t$ is:

$$\frac{\Delta\eta}{\Delta t} = \frac{1}{\rho_{dry}} \cdot (-E) = -\frac{1}{\rho_{dry}} \cdot M \cdot (\tau_{cw,rms} - \tau_e) \tag{12}$$

where E (kg/m^2/s) is the erosion rate. From Eq. (12), the erosion coefficient, M, can then be determined by:

$$M = -\frac{\Delta\eta}{\Delta t} \cdot \rho_{dry} \cdot \frac{1}{\tau_{cw,rms} - \tau_e} \tag{13}$$

where ρ_{dry} is set to 800 kg/m^3. For each time step $\Delta t = t_{i+1} - t_i$, the depth z is defined as the difference between the bed level at t_i with the original bed level. Regression of τ_e and z is used to determine the τ_e value at this certain depth z. $\tau_{cw,rms}$ at t_i is calculated using Eq. (2). The bed level η and its change rate $\Delta\eta/\Delta t$ are obtained from ADV measurements. The vertical distribution of M is then plotted from pairs of M and z.

4. Results

4.1. Tides and waves

Fifty tides were measured during the measurement period (Fig. 2b). A storm event occurred from May 6 to 12. A period of strong onshore winds is referred as a storm period in this paper (Fig. 2a). The difference between the measured and predicted water levels indicated that the average storm surge was 0.4 m and the maximum value was 0.7 m (Fig. 2b). Neap tides that coincided with the storm surge led to continuous inundation at the lowest site A1, which had a water depth of approximately 0.5 m at low water.

The significant wave heights (H_s) at Site A1 were larger during the storm period (average of 0.13 m) than during normal weather (average of 0.04 m) (Fig. 2d). The maximum H_s was 0.34 m on May 9. According to the wave breaking index ($H_s/h > 0.6$ for breaking waves; Battjes and Stive, 1985), the waves at the three sites were nonbreaking for the majority of the measurement period. The waves at Site A1 were on the verge of breaking at low water during the storm period (Fig. 4).

4.2. Bed shear stresses, bed level changes and suspended sediment concentration

In calm weather, the average $\tau_{cw,rms}$ values increased from 0.08 Pa at Site A3 to 0.18 Pa at Site A1. The $\tau_{cw,rms}$ values at Sites A2 and A3 were less than the estimated τ_e from sediment characteristics and Eq. (9) of the surface sediment (Table 2), which implies minor erosion (Fig. 2h). At Site A1, the bed shear stress was slightly larger than computed τ_e based on Eq. (9). The impact of the diatoms is however neglected in this estimation. Because of the presence of the diatoms, which played a role in stabilizing the bed, no obvious bed degradation occurred at Site A1 during this period (see the discussion in Section 5.3).

The bed level variations differed significantly between Site A1 and Site A3. During the storm period, bed degradation was most pronounced at Site A1 (Fig. 2h), where the bed level degraded by 12 cm. Site A1 showed a stepwise variation of the bed level. Bed degradation occurred during very shallow water, which took approximately 20% of the tidal cycle. No significant variations were found for the other 80%, when the water depth was relatively high (Fig. 3a). Much less degradation took place at Sites A2 and A3. Bed shear stresses at sites A2 and A3 were not measured during the storm period due to battery shortage.

The measured near-bed SSC (c_b) at Site A1 varied from 0.01 kg/m^3 to 5.9 kg/m^3 with an average value of 0.5 kg/m^3 (Fig. 2f). Near-bed SSC peaks during calm high slack water denote deposition, while peaks at low water during the storm is related to erosion (also see Fig. 5).

4.3. Diatom biomass

A visible diatom biofilm covered the mudflat before the storm. Near Site A2, the average chlorophyll *a* concentration of the surface 2-mm sediment layer was 180 mg/m^2, which was similar to the value of the reference sample with a high diatom biomass (208 mg/m^2; Fig. 6). Unfortunately, no measurements of diatom biomass were made after the storm.

4.4. Erosion thresholds and erosion coefficient

Time series of the bed level and maximum bed shear stress $\tau_{cw,\max}$ for the storm period on May 11 (T26 and T27) are shown in Fig. 7a and b, respectively. The deposition rate during each shallow water stage, when the bed starts to degrade, was negligible because $\tau_{cw,rms}$ became larger than the critical shear stress for erosion, τ_e, at this depth. After this degradation period, the bed stopped degrading and returned to a relatively stable state when $\tau_{cw,rms}$ decreased to a certain threshold. These two thresholds, at which the system began to change its state from relatively stable to an erosional state and from the erosional state to a relatively stable state, can approximately represent the τ_e values of the sediment at the bed levels (Fig. 7; Andersen et al., 2007). It means that in situ measurements provide the possibility to measure τ_e very frequently. This approach is based on the assumption that deposition is negligible during stormy weather. Each deeper layer of the bed sediments exposed to the flow, as new surface layer, is better consolidated.

The τ_e values increased from 0.10 Pa at the sediment surface to 1.13 Pa at a depth of 0.12 m (Fig. 8a). The surface sediment was often freshly deposited mud. The water content of the surface sediment decreased from the lowest site, Site A1, to the highest site, Site A3. Considering the cohesive force reflected by the grain size distribution, the τ_e values has little difference from A1 to A3 (Table 2). This is probably because the Kapellebank mudflat is very short and flat, leading to a cross-shore homogeneous distribution of sediment properties.

Bed degradation of only 3 mm occurred during the ebb stage of the tidal cycle on May 22 (T48), when the wind turned onshore with a speed of 8.4 m/s (Figs. 2a and 7d). The erosion threshold τ_e was 0.13 Pa, which represents freshly deposited sediment, and was close to the value obtained by Eq. (9). The bed level changes at Sites A2 and A3 were low during tidal inundations, so determining the erosion threshold of the sediment at these sites is difficult. This condition is identical to the condition at Site A1 before the calm conditions.

The application of Eq. (13) with the results of A1 shows that the M value within the uppermost 12 cm of the sediment layers varied from 0.03×10^{-3} to 7.9×10^{-3} s/m with an average value of 1.9×10^{-3} s/m. There was no obvious trend in M in the uppermost 12 cm of the sediment bed (Fig. 9). As no significant erosion events took place for the higher parts of the flat (A2 and A3), no value for M could be obtained for these locations.

5. Discussion

5.1. Sensitivity of the mud bed to erosion

Studies of morphological changes on an open tidal mudflat showed that the distribution of erosion and accretion zones depends on the

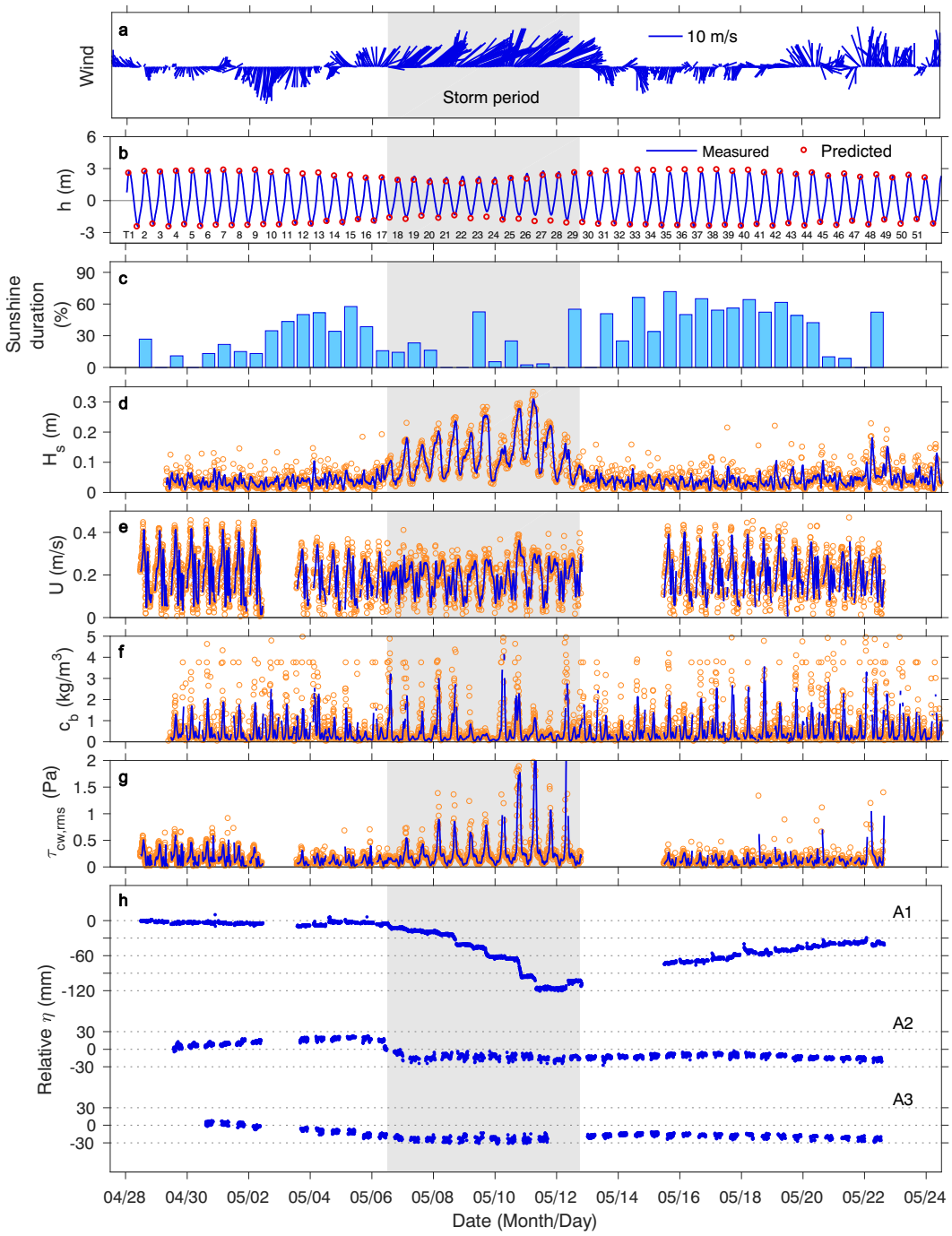

Fig. 2. Time series of the (a) wind vectors, (b) measured water level (h) and predicted high and low water levels at the Hansweert gauge, (c) sunshine duration, (d) significant wave height (H_s), (e) current speed (U), (f) suspended sediment concentration (c_b), (g) root-mean-square bed shear stress ($\tau_{cw,rms}$), and (h) bed level changes. (d–g) are based on measurements (orange circles) at Site A1; running-smooth (blue lines) is used to emphasize the tidal-cycle variability. Continuous numbers in panel (b) indicate the order of the tidal cycles, e.g., T7 refers to the seventh tidal cycle. Each tidal cycle counts from a low water to the next.

Table 2
Calculated critical shear stress for erosion (τ_e) of surface sediment along the cross-shore profile.

Site location	Elevation (m NAP)	d_{50} (μm)	W (%)	Mud content (%)	$\tau_{e,cal}$ (Pa)
A1	−1.25	20.2	148	83	0.086
A2	−0.98	20.4	130	84	0.093
A3	−0.25	30.6	106	76	0.090

tidal range and that lower flats are often eroded during storm events (Fan et al., 2006). Our study shows a similar pattern: significant bed erosion occurred during wind events around the lower flat (Site A1), whereas the middle flat (Sites A2 and A3) experienced much smaller variations in the bed level (Fig. 2h). Studies have demonstrated that these erosion zones coincide with high-wave-energy or wave-breaking zones because near-breaking or breaking waves generate turbulent flows that stir up substantial bed material (Shi and Chen, 1996; Fan et al., 2006; de Vries et al., 2008).

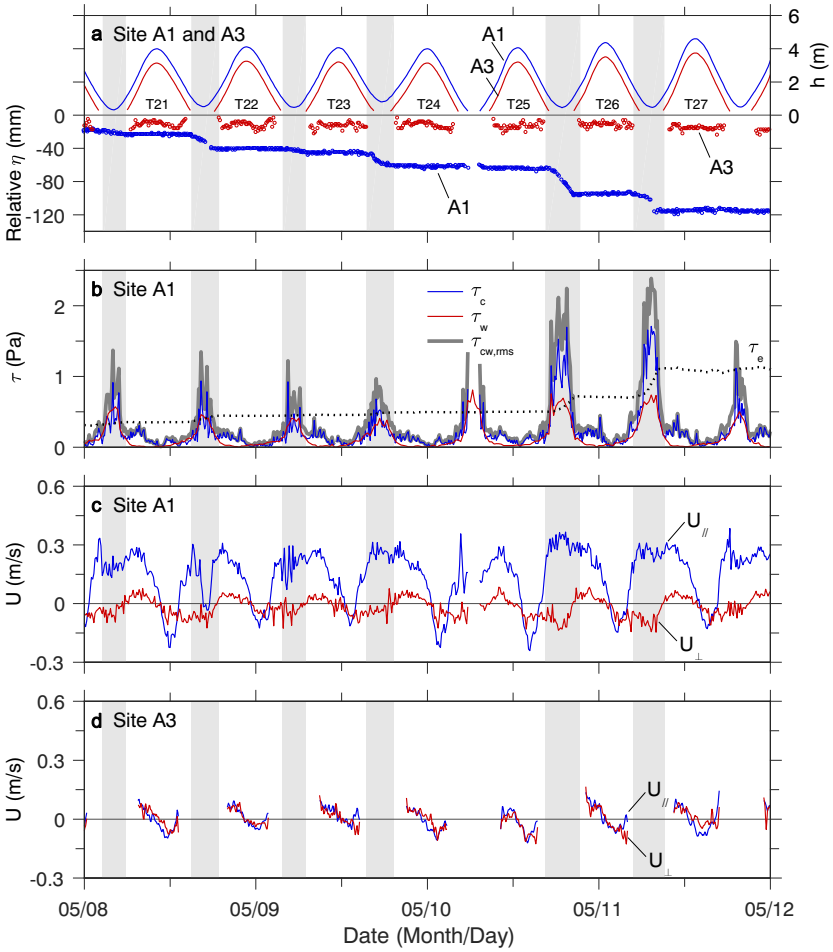

Fig. 3. Time series (detail of Fig. 2) of the (a) water depth (h), and relative bed level (η); (b) bed shear stress due to currents (τ_c), waves (τ_w), combined currents and waves ($\tau_{cw,rms}$), critical shear stress for erosion (τ_e) at the corresponding depth below the original bed level; (c) and (d) currents ($U_{//}$: longshore component, positive values represent eastward velocities; $U_{\perp}$: onshore component, positive values represent onshore velocities). The shallow water stages with obvious bed degradations at Site A1 are highlighted with grey backgrounds.

Various high-temporal-resolution bed-level measurements have shown that significant bed erosion often occurs under very shallow conditions (i.e., water depths <0.25–0.7 m; O'Brien et al., 2000; Andersen et al., 2006; Shi et al., 2015). At Site A1, the waves had a high probability of breaking over 6.4% in the storm period, mostly in shallow waters. The ratio of the significant wave height to the water depth exceeded 0.60 and sometimes surpassed the threshold value for wave breaking of 0.73 (Battjes and Stive, 1985). Consequently, significant erosion occurred during very shallow stages (Fig. 3).

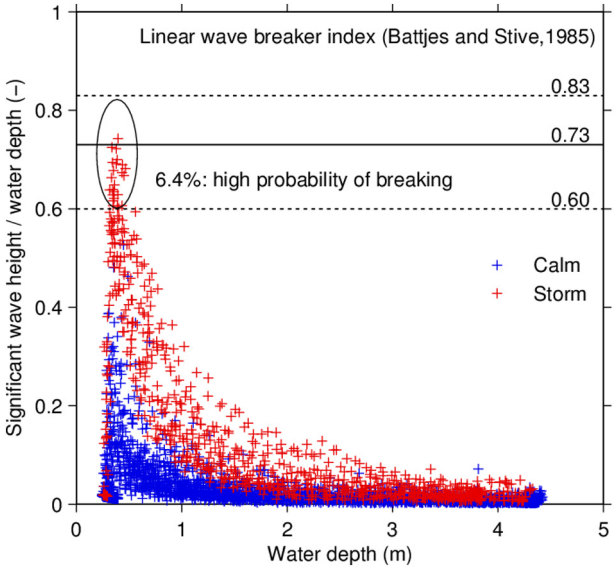

Fig. 4. Ratio of significant wave height over water depth at Site A1.

In summary, significant bed erosion tended to take place at Site A1 rather than in the upper area for the following reasons: (1) the bed was exposed to large hydrodynamic forces caused by wind/storm events; and (2) the duration of the very shallow water stage is long enough that large bed shear stresses continuously affect the bottom and can even lead to wave breaking. Combining the two aspects, the bed at the elevation just below low tide is more dynamic. Note that this location of the bed affected by strong hydrodynamic forces during shallow water stage also shifts seaward or landward near the mean low water level, because the low tide varies with spring-neap cycle. However, erosion during very shallow water is difficult to detect with field measurements. Acoustic instruments are generally applied facing downward to obtain the bed position using ultrasonic echo-ranging (Jestin et al., 1998; O'Brien et al., 2000; Saulter et al., 2003; Andersen et al., 2006; Zhu et al., 2014). These devices cannot make measurements when the water surface drops below the echo transmitter (i.e., water depth < 0.3–0.45 m). Erosion process under very shallow conditions is also often ignored by numerical models. There is a threshold depth below which the model regards the bed as dry and stops the simulation. This threshold depends on the tidal range and the simulation time step and is often set to centimeters to tens of centimeters (Deltares, 2010).

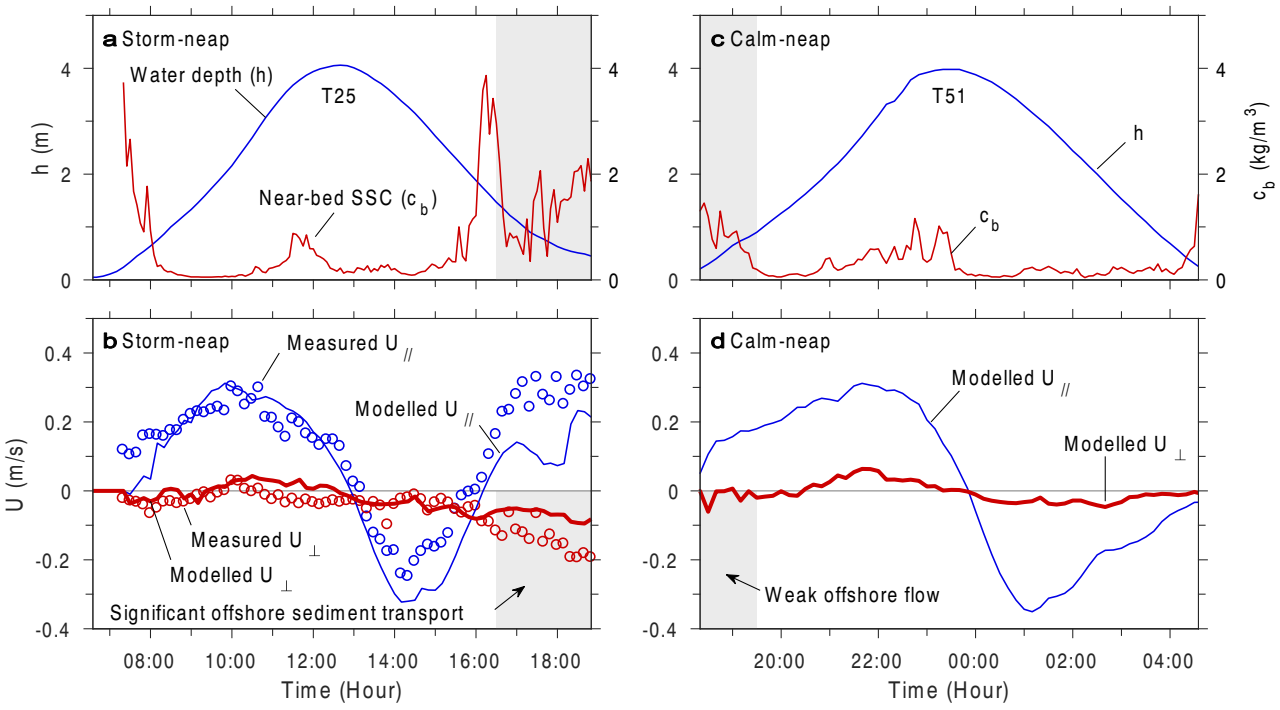

Fig. 5. Time series of the water depth, near-bed suspended sediment concentration (c_b), and long-shore ($U_{//}$) and cross-shore ($U_{\perp}$) velocities in a storm-neap tidal cycle (a, b) and a calm-neap tidal cycle (c, d) at Site A1.

5.2. Effect of the flow pattern on sediment transport during a storm

Bed erosion has been considered to be increased by the wave-induced bed shear stress, which is enhanced by storms (Janssen-Stelder, 2000; Yang et al., 2003; Fan et al., 2006; Dalyander et al., 2013). In recent years, the influence of wind-driven currents and turbulence has been emphasized (Banerjee et al., 2015; Su et al., 2015). In this study, τ_w increased significantly during the shallow waters of the storm neap tides. However, τ_w surpassed τ_e by a limited amount and was sometimes even smaller than τ_e. Fig. 3b shows that τ_{cw} was dominated by the current-induced component (τ_c) during significant erosion periods because strong flows occurred during the low tides (Figs. 3c and 5b). As estimated in de Vet et al. (2018), the wind-induced flow velocity can reach a value of the wind speed divided by ~40. The storm wind-induced turbulence generated at the water surface may also enhance τ_c and transfer it to the bottom layer (Su et al., 2015). Note that τ_c was obtained using the bulk turbulent strength $\overline{w_t^2}$, so the turbulence from bottom friction and surface momentum are not distinguished.

The tidal wave was nearly standing in the study area because low flow velocities occurred near the high and low water levels (Fig. 5). However, the velocity series during the storm neap tides in both the long-shore and cross-shore directions exhibited asymmetry: the ebb flow turned to the east when the ebb peak began, and the velocity was high; meanwhile, strong offshore flow occurred during the low tides (Fig. 5b). Maan et al. (2018) simulated the flow velocities of this case study. The numerical model simulations for the two neap tide periods with and without the effect of storms (Fig. 5) show that the velocity asymmetry was caused by the wind rather than the spring neap cycle. This pattern was absent in the simulated velocities of the calm neap tides (Fig. 5d). The modified flow in the shallow water stages was different from the normal wind-driven flow in the open sea; it was a result of the interaction between the wind and the tidal flat-channel topography. The occurrence of this modified flow pattern at the flat-channel interface further increased the instability of the bed in this area (Fig. 11).

The higher flow velocities during the shallow water periods also played an important role in the cross-shore sediment transport. In calm weather, SSC peaks appeared during the flood peak stage, so the net cross-shore sediment fluxes were onshore during calm

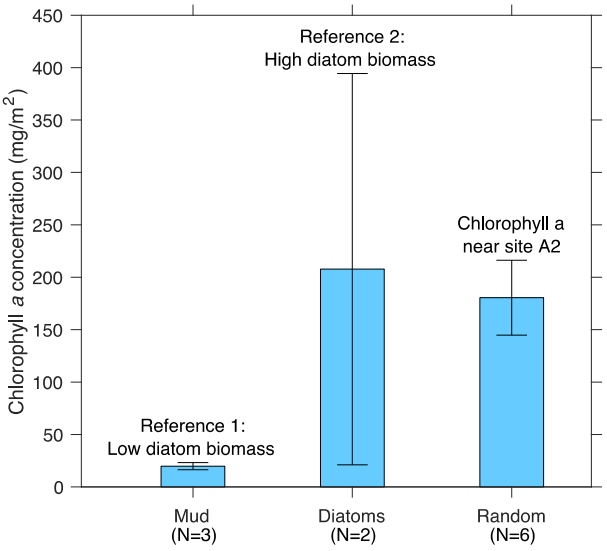

Fig. 6. Chlorophyll *a* concentration near Site A2 at Kapellebank mudflat. The blue bars indicate the mean value, and the error-bars represent the standard deviation. The two references were from the samples collected at nearby points that visually appeared to have high and low diatom biomass.

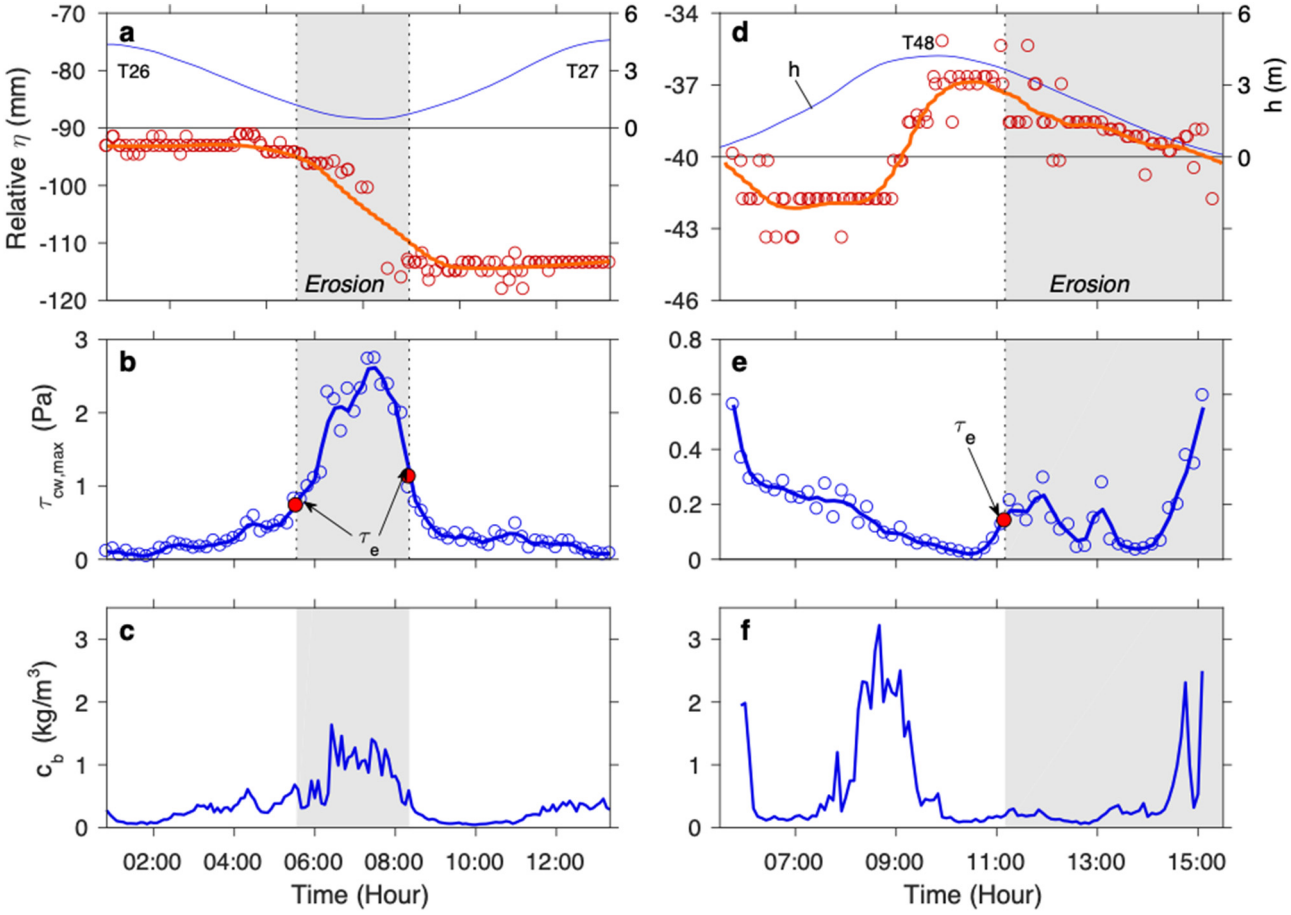

Fig. 7. Examples of determining the critical shear stress for erosion (τ_e) and deposition (τ_d) from the ADV-measured bed level variability and maximum bed shear stress ($\tau_{cw,max}$) under storm conditions (a, b) and calm conditions (d, e) at Site A1. Each solid line is the trend line of the observations. (c) and (f) are time series of near-bed SSC of each tidal cycle.

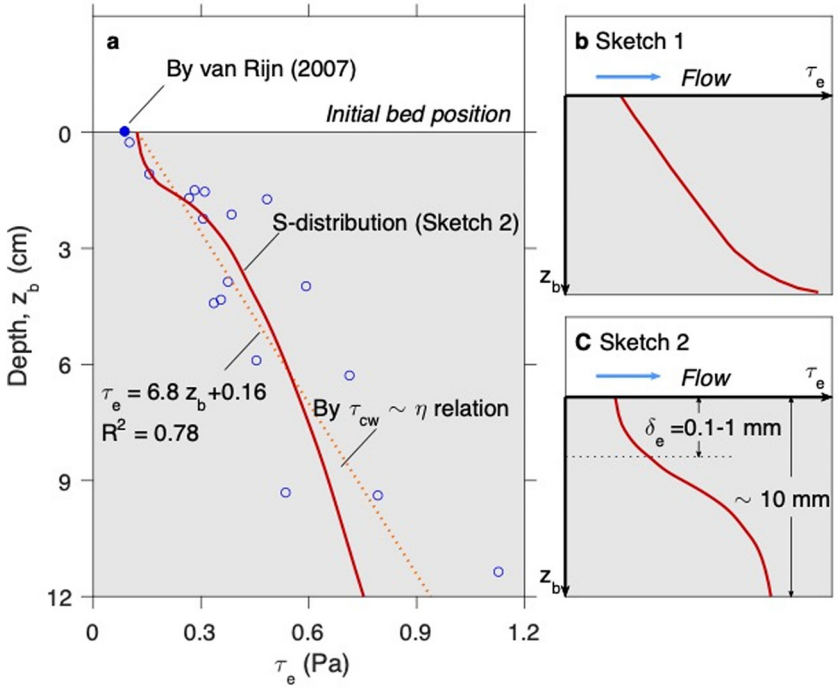

Fig. 8. (a) Vertical distribution of abiotic τ_e. The schematic diagrams of τ_e's vertical distribution are redrawn after (b) Whitehouse et al. (2000; Sketch 1) and (c) Winterwerp et al. (2012; Sketch 2). The δ_e in Sketch 2 is the erodible depth within which the sediment is easily eroded in the form of surface erosion.

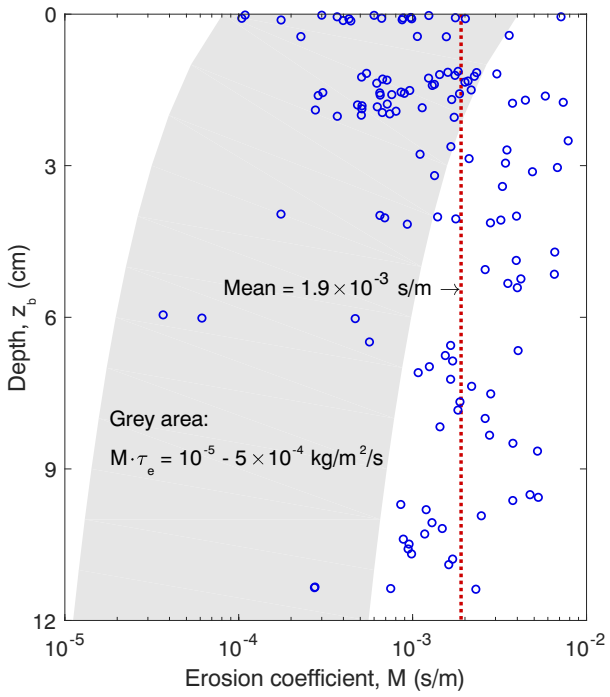

Fig. 9. Vertical distribution of erosion coefficient (M) of this study (circles), and suggested values provided by Winterwerp and van Kesteren (2004; grey area).

tidal cycles (Fig. 10). In stormy weather, the SSC peaks during the low tides were much larger than those during high water periods (Fig. 5a). Increased flows enhanced the bed shear stress, which eroded substantial amounts of sediment and carried it away, leading to net offshore sediment transport (Fig. 10). This net sediment transport model is consistent with the results from open mudflats (Bassoullet et al., 2000; Yang et al., 2003; Fan et al., 2006) and agrees with the theory that sediment moves from high-energy areas to low-energy areas along the energy gradient (Yang et al., 2003; Friedrichs, 2011).

5.3. Abiotic and biotic effects on τ_e of surface sediment

Currently, determinations of the τ_e value of surface mud, which is freshly deposited and has a high water content, are based on empirical formulae that incorporate the water content (Taki, 2001), bulk density (Mehta, 1988; Mitchener and Torfs, 1996), or dry density (Delo and Ockenden, 1992; Whitehouse, 2000). These three sediment characteristics are transferable. Recently, mud or silt fraction and cohesion have been taken into account (van Ledden, 2003; van Rijn, 2007). When using Eq. (9), the τ_e of the surface sediment at Site A1 was estimated to be 0.09 Pa. This value matches that obtained by reading the τ_{cw} and η time series for sediment at $z_b = 2.5$ mm in the erosion stage and the freshly deposited mud in the recovery stage. Here, z_b is the depth beneath the sediment surface and is positive downward.

In addition, a visible diatom biofilm was present on the mudflat, whose effect was not considered in the empirical formulae. Andersen et al. (2010) found that τ_e increased linearly with the EPS content. The chlorophyll a concentration is also a good proxy for the diatom biomass on bare mudflats (Riethmüller et al., 2000; Kazemipour et al., 2012). Riethmüller et al. (2000) found a high correlation coefficient between τ_e and the chlorophyll a concentration (<100 mg/m^2). In this study, the calculated mean $\tau_{cw,rms}$ and the mean value of uppermost 10% $\tau_{cw,rms}$ of the surface sediment in the pre-storm stage were 0.17 Pa and 0.46 Pa, respectively. These values are higher than the abiotic τ_e value, which was calculated to be 0.09 Pa using Eq. (9). Bed erosion was expected to occur, but the bed level measurements showed no significant decrease (Fig. 2h). Considering the surface thin layer of sediment has little chance to consolidate as it suffers from tides and waves, these results suggest that τ_e increased to at least 0.46 Pa due to the existence of a diatom biofilm. On a mudflat in the East Frisian Wadden Sea, τ_e reached 1.2 Pa when the chlorophyll a concentration was 45 mg/m^2 (Andersen et al., 2010). So, we suggest that the diatom distribution should be included in models to improve the understanding of the temporal variability in sedimentation (Fig. 11), whose magnitude might be sufficient to affect the mud balance of the estuary (Herman et al., 2001).

5.4. Vertical distribution of τ_e

The value of τ_e increases with depth beneath the sediment surface because deeper sediment layers are better consolidated (e.g., higher bulk density; Townsend and McVay, 1990; Gomez

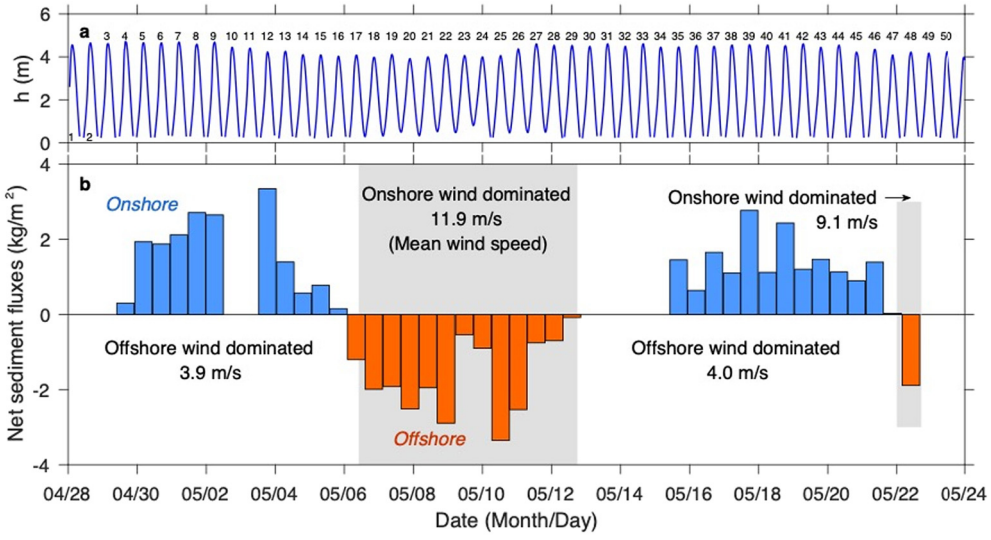

Fig. 10. (a) Water depth (h), and (b) net sediment transport fluxes per unit width at 15 cm above the (original) bed at Site A1. Net offshore sediment transport occurred when strong onshore winds occurred, while net onshore sediment transport occurred in calm weather under spring tides.

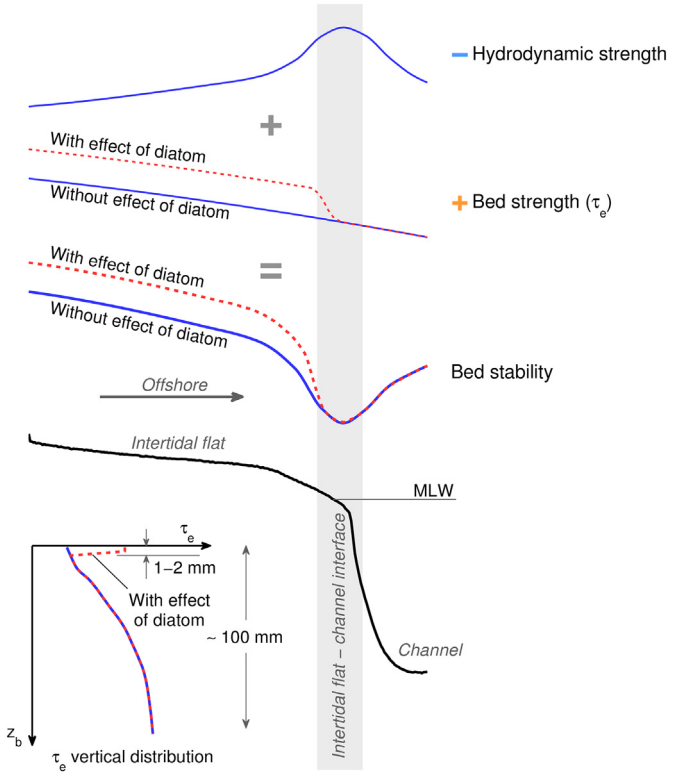

Fig. 11. Schematic diagram of the bed stability distribution of a tidal mudflat in both the cross-shore and vertical dimensions. The bed stability decreases from the higher to lower tidal flat as bed strength (τ_e) decreases and the hydrodynamics forces increases. The bed stability is further weakened at the interface between the intertidal flat and the channel because wave-breaking and complex flow structures have a high probability of occurring in this area. Vertically, τ_e increases downwards, and increases at a smaller gradient towards the deeper bed from a certain depth. The bed stability distribution in both dimensions is changed by the diatoms, because they enhance τ_e of the surface sediment.

and Amos, 2005; Zhou et al., 2016). Mehta and Partheniades (1982) described that bed degradation in a stratified bed stops when the bed shear stress equals the critical shear stress. The vertical distribution of τ_e explains this depth-limited erosion (also called supply-limited erosion). However, how τ_e increases with depth has been less commonly reported than τ_e estimations for surface sediment.

In situ measurements have shown the τ_e distribution of undisturbed sediment beds. In the flume experiment by Mehta and Partheniades (1982), a bed deposited from suspension under a small shear stress was similar to a natural sediment bed. The variation of τ_e with z_b showed a tilted-S distribution (Fig. 8c) within 1–2 cm. After consolidation for 144 h, τ_e reached 0.6 Pa at 1.4 cm below the sediment surface. This tilted-S distribution and length scale were later schematized by Mehta and Partheniades (1982) and Winterwerp et al. (2012). Another schematic τ_e distribution showed a linear increase with z_b (Delo and Ockenden, 1992) (Fig. 8b). Statistical analysis of our data shows that τ_e and z_b have a linear relationship with the correlation coefficient of 0.78 (Fig. 8a). However, τ_e is expected to become constant in the substrate layer rather than increase to an infinite depth. Therefore, an S-distribution for τ_e (Fig. 8c), which was proposed by Winterwerp et al. (2012), is suggested. This implies a finite value for the deeper layer. Note that the length scale of τ_e vertical variability could depend on the dynamic of local bed. The thicker the active layer, the deeper where τ_e is expected to become constant.

The sediment beds in some laboratory flume studies were similar to but still differed from natural undisturbed sediment beds. Instead, an in situ benthic annular flume has been used to study the resuspension characteristics (Amos et al., 1992; Thompson et al., 2011). They generated hydrodynamic forces within the flume, whereas this study took advantage of natural tide and wave forces. In addition, some of the aforementioned studies were restricted to the τ_e distribution in the uppermost centimeters, whereas this study extended this range to 12 cm (Fig. 8a). However, Fig. 8a shows that τ_e has an increasing trend at $z_b = 12$ cm, which indicates that the substrate's better consolidated layer, where τ_e is expected to approach a constant, has not yet been reached. In addition, scattered values of τ_e in Fig. 8a are found at the depth where the bed level has a clear inflection from a stable status to rapid degradation (Figs. 3a, b, 7a and b). This bed-level variation pattern sometimes does not occur naturally. For example, continuous bed degradation has been found throughout the tidal submergence during strong wind conditions (Zhu et al., 2014), or there may be no obvious variation in the bed-level changes, such as at sites A2 and A3 in this study. In this case, flume studies, which are safe and controllable, are sometimes better than in situ measurements.

5.5. Vertical distribution of M

The M value of mud beds is often considered to be constant but actually varies by orders of magnitude (Table 3). This study used in situ measurement datasets to deduce the M values, according to Eq. (13), of an undisturbed sediment bed. The M values for the surficial sediments are consistent with those in the literature in terms of their order of magnitude (Table 3). However, comparing the vertical distribution of M values is difficult because previous studies only showed the results within the uppermost 1–2 cm. Our study extended the vertical M distribution to the uppermost 12 cm, which showed no significant variation in M with z_b in sediment layers that could be eroded under storm conditions. This means that in the erosion equation $E = M(\tau_{cw} - \tau_e)$ for $\tau_{cw} > \tau_e$, M can be regarded as a constant in the vertical dimension, which is described by most current erosion models.

Partheniades' equation is currently the most commonly used equation in the erosion modules of morphodynamic models, likely because of its simplicity. Eq. (1) shows that there are two forms of the erosion equation, in which two erosion parameters, M (or M') and τ_e, need to be specified. Our finding of a constant vertical M distribution suggests that $E = M(\tau_{cw} - \tau_e)$ for $\tau_{cw} > \tau_e$ is more applicable. This means that in a given area, only one varying erosion parameter, τ_e, must be specified, whereas in $E = M'(\frac{\tau_{cw}}{\tau_e} - 1)$ (for $\tau_{cw} > \tau_e$), both $M' = M \cdot \tau_e$ and τ_e are varying parameters that must be individually treated.

6. Conclusions

The erosion potential (i.e., bed stability) of a mudflat is essential to the prediction of morphological changes and sediment budgets. In this paper, the erodibilities of an undisturbed semi-enclosed mudflat in both the cross-shore and vertical dimensions were determined using in situ measurements. The bed stability decreases in the offshore direction as τ_e decreases, and the hydrodynamic forces increase from the higher to lower tidal flat. Because wave-breaking and complex flow structures have a high probability of occurring at the interface between the intertidal flat and the channel, bed stability is significantly weakened in this area.

This study shows for the first time by means of in situ measurements that the vertical length scales of the variations in τ_e and M of an undisturbed cohesive sediment bed have been measured towards a relatively well-consolidated layer. This in situ method provides a possibility to measure τ_e very frequently, and for different layers of bed sediments.

Table 3
Comparison of bed sediment characteristics and erosion parameters — critical shear stress (τ_e) and erosion coefficient (M) — of the muds in the selected literatures and the present study.

Sample remarks	d_{50} (um)	ρ_b (kg/m^3)	P_{mud} (%)	τ_e (Pa)	M (10^{-3} s/m)	$M' = M \cdot \tau_e$ (10^{-4} kg/m^2/s)	Reference
Kaolinite in tap water	1	1093–1218	100	–	–	0.13	Mehta and Partheniades (1982)
Kaolinite in salt water	1	1116–1239	100	–	–	0.07	
HR Wallingford – Grangemouth	–	1370	89–90	–	0.5–1.4	–	Whitehouse et al. (2000)
HR Wallingford – Harwich	–	1250	88–95	–	0.7	–	
HR Wallingford – Hong Kong	–	–	65–80	–	0.6–1.5	–	
HR Wallingford – Ipswich	–	1320	–	–	0.9–3.0	–	
HR Wallingford – Kelang	–	–	65–80	–	0.2–0.9	–	
HR Wallingford – Kingsnorth	–	1375	64	–	0.7	–	
HR Wallingford – Medway	–	1220	80	–	0.7	–	
HR Wallingford – Mersey Eastham	–	1140	80	–	0.5	–	
HR Wallingford – Poole	–	1500	80–85	–	0.7–1.4	–	
HR Wallingford – Tees Seal Sands	–	1550	75	–	0.2–1.4	–	
HR Wallingford – Tees dredged	–	1430	75	–	0.5–1.8	–	
Jacobs et al. (2011) test	–	1784	16	0.4	9	36	van Prooijen and Winterwerp (2010)
Amos et al. (1992) test	–	1500	80	2.35	3.4	80	
Ketelmeer – measured	7.3	1167–1626	–	0.2–2.1	0.0006–4.2	1.9–8.4	Winterwerp et al. (2012)
Ijmuiden – measured	2.5	1127–1610	–	1.0–1.3	0.0009–1.9	12–19	
Kembs – measured	21	1512	–	2.4	1.3	31	
Ketelmeer – computed	7.3	1167–1626	–	0.2–2.1	0.004–0.52	1.0–2.8	
Ijmuiden – computed	2.5	1127–1610	–	1.0–1.3	0.003–0.46	2.9–4.6	
Kembs – computed	21	1512	–	2.4	0.17	4.1	
Kapellebank – A1	20	1492	83	0.1–0.8	0.03–9.1	0.09–29	This paper

Without diatoms, τ_e increased at a smaller gradient towards the deeper bed from a depth of 1.5 cm, whereas M can be regarded as being constant with depth in the linear erosion equation $E = M(\tau_{cw} - \tau_e)$ for $\tau_{cw} > \tau_e$.

There is a strong indication that the diatoms increase the critical bed shear stress for erosion of the surface sediment on intertidal flats by several times. They change the vertical distribution of the bed stability by enhancing τ_e of the surface sediment.

Based on our results, the following model improvements for predicting morphological changes of tidal mudflats are suggested: (1) very shallow conditions should be better simulated by not omitting these periods; (2) the vertical distribution of τ_e should be considered; erosion rates can be overestimated, especially during extreme events, because exposure of the deeper well-consolidated layer likely occurs; and (3) an appropriate description of the effect of diatoms should be considered as part of the bottom boundary condition.

Acknowledgments

This study was supported by the project "Coping with deltas in transition" within the Programme of Strategic Scientific Alliances between China and The Netherlands (PSA), financed by the Chinese Ministry of Science and Technology (MOST; project no.: 2016YFE0133700) and Royal Netherlands Academy of Arts and Sciences (KNAW; project no.: PSA-SA-E-02). It was also funded by the Netherlands Organisation for Scientific Research NWO (NWO-JSTP: 842.00.007), the Natural Science Foundation of China (41576092), and the NSFC-Shandong Joint Fund for Marine Science Research Centers (U1606401). We thank Xianye Wang, Jinghua Gu, Chao Guo, and staff from TU Delft, Rijkswaterstaat, NIOZ, UNESCO-IHE and Deltares for their assistance in this survey; Irene Colosimo for calibrating turbidity sensors. We also thank Shore Monitoring & Research for measuring the detailed bathymetry of Kapellebank mudflat before the field campaign.

Appendix A

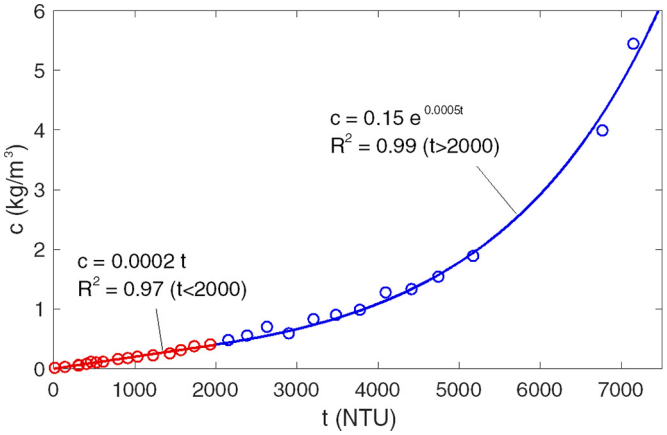

Fig. A1. Relation between fluorometer measured turbidity (t) and suspended sediment concentration (c). c increased linearly with t in low turbidity condition (t < 2000 NTU); and increased exponentially with t in high turbidity condition ($t \geq 2000$ NTU).

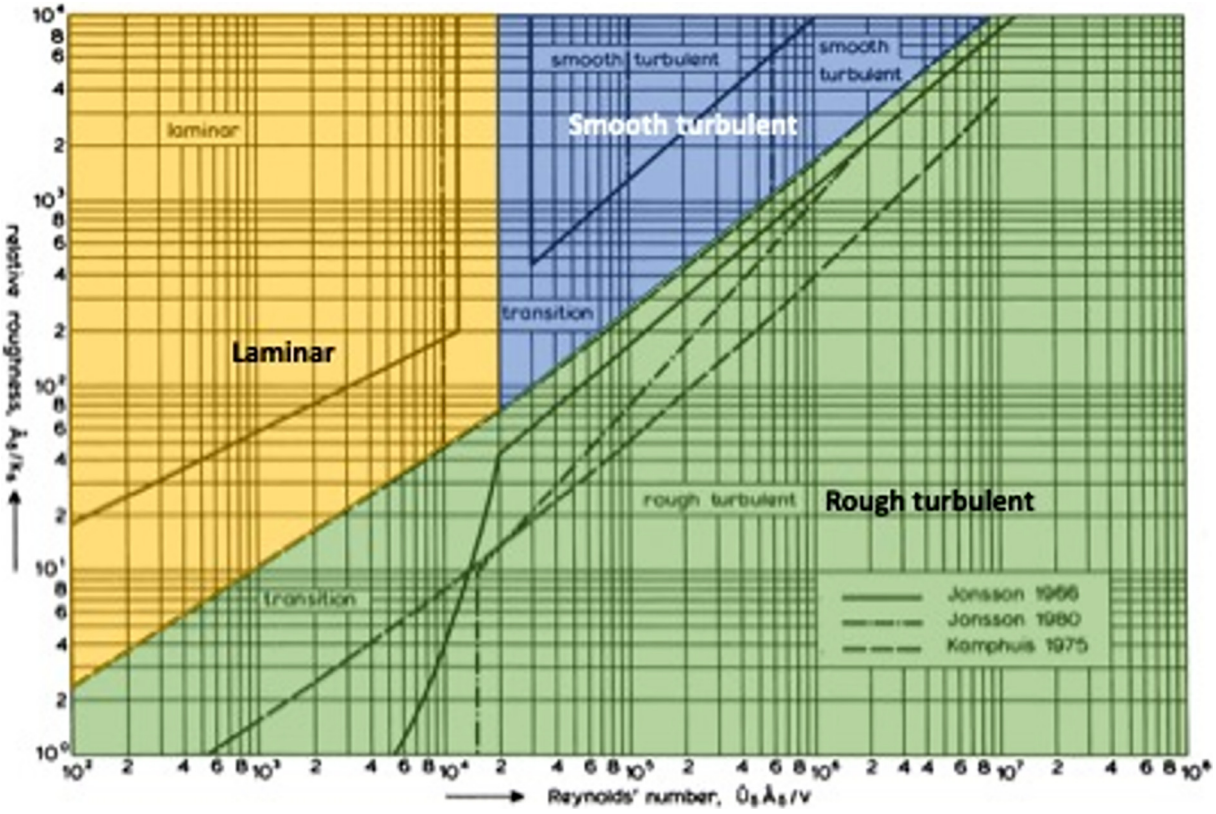

Fig. A2. Definition of hydraulic regimes in Eq. (7) calculating wave friction coefficient. (Redrawn from Fig. 2.3.2 of van Rijn, 1993).

References

Amos, C.L., Daborn, G., Christian, H., Atkinson, A., Robertson, A., 1992. In situ measurements on fine-grained sediments from the Bay of Fundy. Mar. Geol. 108 (2), 175–196.

Amos, C.L., Sutherland, T.F., Zevenhuizen, J., 1996. The stability of sublittoral, fine-grained sediments in a subarctic estuary. Sedimentology 43 (1), 1–19.

Andersen, T.J., Pejrup, M., 2002. Biological mediation of the settling velocity of bed material eroded from an intertidal mudflat, the Danish Wadden Sea. Estuar. Coast. Shelf Sci. 54 (4), 737–745.

Andersen, T.J., Lund-Hansen, L.C., Pejrup, M., Jensen, K.T., Mouritsen, K.N., 2005. Biologically induced differences in erodibility and aggregation of subtidal and intertidal sediments: a possible cause for seasonal changes in sediment deposition. J. Mar. Syst. 55 (3–4), 123–138.

Andersen, T.J., Pejrup, M., Nielsen, A.A., 2006. Long-term and high-resolution measurements of bed level changes in a temperate, microtidal coastal lagoon. Mar. Geol. 226 (1–2), 115–125.

Andersen, T.J., Fredsoe, J., Pejrup, M., 2007. In situ estimation of erosion and deposition thresholds by Acoustic Doppler Velocimeter (ADV). Estuar. Coast. Shelf Sci. 75 (3), 327–336.

Andersen, T.J., Lanuru, M., van Bernem, C., Pejrup, M., Riethmueller, R., 2010. Erodibility of a mixed mudflat dominated by microphytobenthos and Cerastoderma edule, East Frisian Wadden Sea, Germany. Estuar. Coast. Shelf Sci. 87 (2), 197–206.

Andersen, T.J., Svinth, S., Pejrup, M., 2011. Temporal variation of accumulation rates on a natural salt marsh in the 20th century - the impact of sea level rise and increased inundation frequency. Mar. Geol. 279 (1–4), 178–187.

Armanini, A., 1995. Non-uniform sediment transport: dynamics of the active layer. J. Hydraul. Res. 33 (5), 611–622.

Austen, I., Andersen, T.J., Edelvang, K., 1999. The influence of benthic diatoms and invertebrates on the erodibility of an intertidal a mudflat, the Danish Wadden Sea. Estuar. Coast. Shelf Sci. 49 (1), 99–111.

Banerjee, T., Muste, M., Katul, G., 2015. Flume experiments on wind induced flow in static water bodies in the presence of protruding vegetation. Adv. Water Resour. 76, 11–28.

Barbier, E.B., Koch, E.W., Silliman, B.R., Hacker, S.D., Wolanski, E., Primavera, J., Granek, E.F., Polasky, S., Aswani, S., Cramer, L.A., Stoms, D.M., Kennedy, C.J., Bael, D., Kappel, C.V., Perillo, G.M.E., Reed, D.J., 2008. Coastal ecosystem-based management with nonlinear ecological functions and values. Science 319 (5861), 321–323.

Bassoullet, P., Le Hir, P., Gouleau, D., Robert, S., 2000. Sediment transport over an intertidal mudflat: field investigations and estimation of fluxes within the "Baie de Marennes-Oleron" (France). Cont. Shelf Res. 20 (12−13), 1635–1653.

Battjes, J.A., Stive, M.J.F., 1985. Calibration and verification of a dissipation model for random breaking waves. J. Geophys. Res. 90 (C5), 9159–9167.

Blum, M.D., Roberts, H.H., 2009. Drowning of the Mississippi Delta due to insufficient sediment supply and global sea-level rise. Nat. Geosci. 2 (7), 488–491.

Bohling, B., 2009. Measurements of threshold values for incipient motion of sediment particles with two different erosion devices. J. Mar. Syst. 75 (3–4), 330–335.

Christie, M.C., Dyer, K.R., Turner, P., 1999. Sediment flux and bed level measurements from a macro tidal mudflat. Estuar. Coast. Shelf Sci. 49 (5), 667–688.

Chu, Z.X., Sun, X.G., Zhai, S.K., Xu, K.H., 2006. Changing pattern of accretion/erosion of the modern Yellow River (Huanghe) subaerial delta, China: based on remote sensing images. Mar. Geol. 227, 13–30.

Costanza, R., de Arge, R., de Groot, R., Farber, S., Grasso, M., Hannon, B., Limburg, K., Naeem, S., Oneill, R.V., Paruelo, J., Raskin, R.G., Sutton, P., van den Belt, M., 1997. The value of the world's ecosystem services and natural capital. Nature 387 (6630), 253–260.

Dalyander, P.S., Butman, B., Sherwood, C.R., Signell, R.P., Wilkin, J.L., 2013. Characterizing wave- and current-induced bottom shear stress: U.S. middle Atlantic continental shelf. Cont. Shelf Res. 52, 73–86.

de Brouwer, J.F.C., Wolfstein, K., Ruddy, G.K., Jones, T.E.R., Stal, L.J., 2005. Biogenic stabilization of intertidal sediments: the importance of extracellular polymeric substances produced by benthic diatoms. Microb. Ecol. 49 (4), 501–512.

de Vet, P.L.M., van Prooijen, B.C., Wang, Z.B., 2017. The differences in morphological development between the intertidal flats of the Eastern and Western Scheldt. Geomorphology 281, 31–42.

de Vet, P.L.M., van Prooijen, B.C., Schrijvershof, R.A., van der Werf, J.J., Ysebaert, T., Schrijver, M.C., Wang, Z.B., 2018. The importance of combined tidal and meteorological forces for the flow and sediment transport on intertidal shoals. J. Geophys. Res.-Earth Surf. 123 (10), 2464–2480.

de Vries, J., van Gent, M.R.A., Walstra, D.J.R., Reniers, A., 2008. Analysis of dune erosion processes in large-scale flume experiments. Coast. Eng. 55 (12), 1028–1040.

Delo, E., Ockenden, M., 1992. Estuarine Muds Manual, HR Wallingford Report SR 309 (Oxfordshire, UK).

Deltares, Deltares (Eds.), 2010. User Manual Delft3D-FLOW. Deltares, Delft, The Netherlands, p. 93.

Dickhudt, P.J., Friedrichs, C.T., Schaffner, L.C., Sanford, L.P., 2009. Spatial and temporal variation in cohesive sediment erodibility in the York River estuary, eastern USA: a biologically influenced equilibrium modified by seasonal deposition. Mar. Geol. 267 (3–4), 128–140.

Dyer, K.R., 1986. Coastal and Estuarine Sediment Dynamics. vol. 1. John Wiley & Sons Inc., p. 173.

Fan, D.D., Guo, Y.X., Wang, P., Shi, J.Z., 2006. Cross-shore variations in morphodynamic processes of an open-coast mudflat in the Changjiang Delta, China: with an emphasis on storm impacts. Cont. Shelf Res. 26 (4), 517–538.

Friedrichs, C.T., 2011. Tidal flat morphodynamics: A synthesis. In: Hansom, J.D., Flemming, B.W. (Eds.), Treatise on Estuarine and Coastal Science. Elsevier.
Ge, J.Z., Shen, F., Guo, W.Y., Chen, C.S., Ding, P.X., 2015. Estimation of critical shear stress for erosion in the Changjiang Estuary: a synergy research of observation, GOCI sensing and modeling. J. Geophys. Res.-Oceans 120 (12), 8439–8465.
Gomez, E.A., Amos, C.L., 2005. Dewatering effects on the erodibility of newly deposited cohesive beds by unidirectional currents. Sedimentology 52 (1), 183–189.
Goodwin, P., Mehta, A.J., Zedler, J.B., 2001. Tidal wetland restoration: an introduction. J. Coastal Res. 27, 1–6.
Gust, G., Morris, M.J., 1989. Erosion thresholds and entrainment rates of undisturbed in situ sediments. J. Coastal Res. 87–99.
Herman, P.M.J., Middelburg, J.J., Heip, C.H.R., 2001. Benthic community structure and sediment processes on an intertidal flat: results from the ECOFLAT project. Cont. Shelf Res. 21 (18–19), 2055–2071.
Houwing, E.J., 1999. Determination of the critical erosion threshold of cohesive sediments on intertidal mudflats along the Dutch Wadden Sea Coast. Estuar. Coast. Shelf Sci. 49 (4), 545–555.
Jacobs, W., Le Hir, P., Van Kesteren, W., Cann, P., 2011. Erosion threshold of sand–mud mixtures. Cont. Shelf Res. 31 (10, Supplement), S14–S25.
Janssen-Stelder, B., 2000. The effect of different hydrodynamic conditions on the morphodynamics of a tidal mudflat in the Dutch Wadden Sea. Cont. Shelf Res. 20 (12–13), 1461–1478.
Jestin, H., Bassoullet, P., Le Hir, P., L'Yavanc, J., Degres, Y., 1998. Development of ALTUS, a high frequency acoustic submersible recording altimeter to accurately monitor bed elevation and quantify deposition and erosion of sediments. Oceans'98 189–194.
Kazemipour, F., Launeau, P., Meleder, V., 2012. Microphytobenthos biomass mapping using the optical model of diatom biofilms: application to hyperspectral images of Bourgneuf Bay. Remote Sens. Environ. 127, 1–13.
Kuijper, C., Steijn, R.C., Roelvink, J.A., van der Kaaij, T., Olijslagers, P., 2004. Morphological Modelling of the Western Scheldt: Validation of Delft3D.
Kuti, E.O., Yen, C.-L., 1976. Scouring of cohesive soils. J. Hydraul. Res. 14 (3), 195–206.
Le Hir, P., Monbet, Y., Orvain, F., 2007. Sediment erodability in sediment transport modelling: can we account for biota effects? Cont. Shelf Res. 27 (8), 1116–1142.
Le Hir, P., Cann, P., Waeles, B., Jestin, H., Bassoullet, P., 2008. Erodibility of natural sediments: experiments on sand/mud mixtures from laboratory and field erosion tests. Proc. Mar. Sci. 9, 137–153.
Lumborg, U., 2005. Modelling the deposition, erosion, and flux of cohesive sediment through Oresund. J. Mar. Syst. 56 (1–2), 179–193.
Maa, J.P.Y., Kwon, J.I., Hwang, K.N., Ha, H.K., 2008. Critical bed-shear stress for cohesive sediment deposition under steady flows. J. Hydraul. Eng.-Asce 134 (12), 1767–1771.
Maan, D.C., van Prooijen, B.C., Zhu, Q., Wang, Z.B., 2018. Morphodynamic feedback loops control stable fringing flats. J. Geophys. Res. Earth Surf. 123, 2993–3012.
McNeil, J., Taylor, C., Lick, W., 1996. Measurements of erosion of undisturbed bottom sediments with depth. J. Hydraul. Eng.-Asce 122 (6), 316–324.
Mehta, A., 1988. Laboratory studies on cohesive sediment deposition and erosion. Physical Processes in Estuaries. Springer, pp. 427–445.
Mehta, A.J., Partheniades, E., 1982. Resuspension of deposited cohesive sediment beds. Coast. Eng. Proc. 1 (18).
Mitchener, H., Torfs, H., 1996. Erosion of mud/sand mixtures. Coast. Eng. 29 (1–2), 1–25.
Neumeier, U., Lucas, C.H., Collins, M., 2006. Erodibility and erosion patterns of mudflat sediments investigated using an annular flume. Aquat. Ecol. 40 (4), 543–554.
O'Brien, D.J., Whitehouse, R.J.S., Cramp, A., 2000. The cyclic development of a macrotidal mudflat on varying timescales. Cont. Shelf Res. 20 (12–13), 1593–1619.
Orvain, F., Le Hir, P., Sauriau, P.G., 2003. A model of fluff layer erosion and subsequent bed erosion in the presence of the bioturbator, Hydrobia ulvae. J. Mar. Res. 61 (6), 823–851.
Orvain, F., Sauriau, P.G., Le Hir, P., Guillou, G., Cann, P., Paillard, M., 2007. Spatio-temporal variations in intertidal mudflat erodability: Marennes-Oleron Bay, western France. Cont. Shelf Res. 27 (8), 1153–1173.
Paterson, D.M., Tolhurst, T.J., Kelly, J.A., Honeywill, C., de Deckere, E., Huet, V., Shayler, S.A., Black, K.S., de Brouwer, J., Davidson, I., 2000. Variations in sediment properties, Skeffling mudflat, Humber Estuary, UK. Cont. Shelf Res. 20 (10−11), 1373–1396.
Ravens, T.M., 2007. Comparison of two techniques to measure sediment erodibility in the Fox River, Wisconsin. J. Hydraul. Eng.-Asce 133 (1), 111–115.
Riethmüller, R., Heineke, M., Kühl, H., Keuker-Rüdiger, R., 2000. Chlorophyll a concentration as an index of sediment surface stabilisation by microphytobenthos? Cont. Shelf Res. 20 (10–11), 1351–1372.
Salehi, M., Strom, K., 2012. Measurement of critical shear stress for mud mixtures in the San Jacinto estuary under different wave and current combinations. Cont. Shelf Res. 47, 78–92.
Sanford, L.P., Halka, J.P., 1993. Assessing the paradigm of mutually exclusive erosion and deposition of mud, with examples from upper Chesapeake Bay. Mar. Geol. 114 (1–2), 37–57.
Saulter, A.N., Russell, P.E., Gallagher, E.L., Miles, J.R., 2003. Observations of bed level change in a saturated surf zone. J. Geophys. Res.-Oceans 108 (C4).
Schünemann, M., Kühl, H., 1993. Experimental investigations of the erosional behavior of naturally formed mud from the Elbe Estuary and Adjacent Wadden Sea, Germany. Nearshore Estuar. Cohesive Sediment Transp. (1–2), 314–330.
Shi, Z., Chen, J.Y., 1996. Morphodynamics and sediment dynamics on intertidal mudflats in China (1961–1994). Cont. Shelf Res. 16 (15), 1909–1926.
Shi, B.W., Wang, Y.P., Yang, Y., Li, M.L., Li, P., Ni, W.F., Gao, J.H., 2015. Determination of critical shear stresses for erosion and deposition based on in situ measurements of currents and waves over an intertidal mudflat. J. Coast. Res. 31 (6), 1344–1356.
Shields, A., 1936. Application of Similarity Principles and Turbulence Research to Bed-load Movement. English Translation of the original German Manuscript. Hydrodynamicss Laboratory, California Institute of Technology (Pub. No 167).
Soulsby, R., 1997. Dynamics of Marine Sands: A Manual for Practical Applications. Thomas Telford.
Soulsby, R., Humphery, J., 1990. Field observations of wave-current interaction at the sea bed. Water Wave Kinematics. Springer, pp. 413–428.
Stapleton, K., Huntley, D., 1995. Seabed stress determinations using the inertial dissipation method and the turbulent kinetic energy method. Earth Surf. Process. Landf. 20 (9), 807–815.
Su, M., Yao, P., Wang, Z.B., Chen, Y.P., Zhang, C.K., Stive, M.J.F., 2015. Laboratory studies on the response of fine sediment to wind. IAHR World Congress 2015. IHAR, the Netherlands.
Taki, K., 2001. Critical shear stress for cohesive sediment transport. In: McAnally, W.H., Mehta, A.J. (Eds.), Coastal and Estuarine Fine Sediment Processes. Elsevier Science, pp. 53–61.
Thompson, C.E.L., Couceiro, F., Fones, G.R., Helsby, R., Amos, C.L., Black, K., Parker, E.R., Greenwood, N., Statham, P.J., Kelly-Gerreyn, B.A., 2011. In situ flume measurements of resuspension in the North Sea. Estuar. Coast. Shelf Sci. 94 (1), 77–88.
Tolhurst, T.J., Black, K.S., Shayler, S.A., Mather, S., Black, I., Baker, K., Paterson, D.M., 1999. Measuring the in situ erosion shear stress of intertidal sediments with the Cohesive Strength Meter (CSM). Estuar. Coast. Shelf Sci. 49 (2), 281–294.
Townsend, F., McVay, M., 1990. SOA: large strain consolidation predictions. J. Geotech. Eng. 116 (2), 222–243.
Tucker, M.J., Pitt, E.G., 2001. Waves in ocean engineering. In: McAnally, W.H., Mehta, A.J. (Eds.), Coastal and Estuarine Fine Sediment Processes. Elsevier Science, pp. 53–61.
van der Wegen, M., Jaffe, B., Foxgrover, A., Roelvink, D., 2017. Mudflat morphodynamics and the impact of sea level rise in South San Francisco Bay. Estuar. Coasts 40 (1), 37–49.
van Ledden, M., 2003. Sand-mud Segregation in Estuaries and Tidal Basins. (PhD Dissertation). Delft University of Technology, the Netherlands.
van Maren, D.S., Winterwerp, J.C., Wang, Z.Y., Pu, Q., 2009. Suspended sediment dynamics and morphodynamics in the Yellow River, China. Sedimentology 56 (3), 785–806.
van Prooijen, B.C., Winterwerp, J.C., 2010. A stochastic formulation for erosion of cohesive sediments. J. Geophys. Res.-Oceans 115, 15.
van Prooijen, B.C., Montserrat, F., Herman, P.M.J., 2011. A process-based model for erosion of Macoma balthica-affected mud beds. Cont. Shelf Res. 31 (6), 527–538.
van Rijn, L.C., 1993. Principles of Sediment Transport in Rivers, Estuaries and Coastal Seas. Aqua Publication, Amsterdam, the Netherlands.
van Rijn, L.C., 2007. Unified view of sediment transport by currents and waves. I: initiation of motion, bed roughness, and bed-load transport. J. Hydraul. Eng.-ASCE 133 (6), 649–667.
Verney, R., Deloffre, J., Brun-Cottan, J.C., Lafite, R., 2007. The effect of wave-induced turbulence on intertidal mudflats: impact of boat traffic and wind. Cont. Shelf Res. 27 (5), 594–612.
Wang, Z., Van Maren, D., Ding, P., Yang, S., Van Prooijen, B., De Vet, P., Winterwerp, J., De Vriend, H., Stive, M., He, Q., 2015. Human impacts on morphodynamic thresholds in estuarine systems. Cont. Shelf Res. 174–183 CSR3681.
Weerman, E.J., Herman, P.M.J., Van de Koppel, J., 2011. Top-down control inhibits spatial self-organization of a patterned landscape. Ecology 92 (2), 487–495.
Whitehouse, R., 2000. Comparison of mud tested at HR Wallingford – erosional/depositional properties determined in laboratory test. In: Wallingford, muds_test_HR (Ed.), Dynamics of Estuarine Muds: A Manual for Practical Applications. Thomas Telford, Victoria.
Whitehouse, R., Soulsby, R., Roberts, W., Mitchener, H., 2000. Dynamics of estuarine muds: A manual for practical applications. Tomas Telford Limited, 1 Heron Quay, London.
Widdows, J., Brinsley, M.D., Bowley, N., Barrett, C., 1998. A benthic annular flume for in situ measurement of suspension feeding/biodeposition rates and erosion potential of intertidal cohesive sediments. Estuar. Coast. Shelf Sci. 46 (1), 27–38.
Widdows, J., Brown, S., Brinsley, M.D., Salkeld, P.N., Elliott, M., 2000. Temporal changes in intertidal sediment erodability: influence of biological and climatic factors. Cont. Shelf Res. 20 (10–11), 1275–1289.
Willows, R.I., Widdows, J., Wood, R.G., 1998. Influence of an infaunal bivalve on the erosion of an intertidal cohesive sediment: a flume and modeling study. Limnol. Oceanogr. 43 (6), 1332–1343.
Winterwerp, J.C., 2007. On the sedimentation rate of cohesive sediment. In: Maa, L.P.S.J.P.Y., Schoellhamer, D.H. (Eds.), Proceedings in Marine Science. Elsevier, pp. 209–226.
Winterwerp, J.C., van Kesteren, W.G.M., 2004. Introduction to the Physics of Cohesive Sediment Dynamics in the Marine Environment. Elsevier Science, Amsterdam, The Netherlands.
Winterwerp, J.C., van Kesteren, W.G.M., van Prooijen, B., Jacobs, W., 2012. A conceptual framework for shear flow-induced erosion of soft cohesive sediment beds. J. Geophys. Res.-Oceans 117, 17.
Wright, S.W., Jeffrey, S.W., Mantoura, R.F.C., Llewellyn, C.A., Bjornland, T., Repeta, D., Welschmeyer, N., 1991. Improved HPLC method for the analysis of chlorophylls and carotenoids from marine phytoplankton. Mar. Ecol.-Progress Ser. 77, 183–196.
Wu, W.M., Perera, C., Smith, J., Sanchez, A., 2018. Critical shear stress for erosion of sand and mud mixtures. J. Hydraul. Res. 56 (1), 96–110.
Yang, S.L., Friedrichs, C.T., Shi, Z., Ding, P.X., Zhu, J., Zhao, Q.Y., 2003. Morphological response of tidal marshes, flats and channels of the outer Yangtze River mouth to a major storm. Estuaries 26 (6), 1416–1425.
Yang, S.L., Li, M., Dai, S.B., Liu, Z., Zhang, J., Ding, P.X., 2006. Drastic decrease in sediment supply from the Yangtze River and its challenge to coastal wetland management. Geophys. Res. Lett. 33 (6).

Yang, S.L., Xu, K.H., Milliman, J.D., Yang, H.F., Wu, C.S., 2015. Decline of Yangtze River water and sediment discharge: impact from natural and anthropogenic changes. Sci. Rep. 5, 14.
Yao, P., Su, M., Wang, Z., van Rijn, L.C., Zhang, C., Chen, Y., Stive, M.J.F., 2015. Experiment inspired numerical modeling of sediment concentration over sand–silt mixtures. Coast. Eng. 105, 75–89.
Yao, P., Hu, Z., Su, M., Chen, Y.P., Ou, S.Y., 2018. Erosion behavior of sand-silt mixtures: the role of silt content. J. Coast. Res. 1171–1175.
Zhou, Z., van der Wegen, M., Jagers, B., Coco, G., 2016. Modelling the role of self-weight consolidation on the morphodynamics of accretional mudflats. Environ. Model. Softw. 76, 167–181.
Zhu, Q., Yang, S., Ma, Y., 2014. Intra-tidal sedimentary processes associated with combined wave–current action on an exposed, erosional mudflat, southeastern Yangtze River Delta, China. Mar. Geol. 347 (0), 95–106.
Zhu, Q., van Prooijen, B.C., Wang, Z.B., Ma, Y.X., Yang, S.L., 2016. Bed shear stress estimation on an open intertidal flat using in situ measurements. Estuar. Coast. Shelf Sci. 182 (Part A), 190–201.